Analysis of Thermal Strains in Composite Integral Armor

V.Y. Yu, C.T. Jagmin, and J. G. Kohl
Department of Civil and Mechanical Engineering, United States Military Academy, West Point, NY 10996-1792

T. A. Bogetti, S. C. Wolf, C. F. Yen, and C. Krauthauser
Army Research Laboratories, Aberdeen Proving Grounds, MD 21005

C. Herbein and H. Mehling
Center for Composite Materials, University of Delaware, Newark, DE 19716

The Army's Future Combat System (FCS) requires a lightweight alternative to the current M1 series Main Battle Tank. In order to replace the M1 series armor, extensive testing of ballistics, survivability, and structural integrity must be performed on the FCS's composite armor. Nested within structural integrity analysis, the thermal properties of armor must be investigated to ensure the equipment is able to be deployed in extreme climates. In this paper, a thermal analysis of proposed FCS armor specimens was conducted to compare the thermal strains in several composite material recipes. Titanium, aluminum, and a S2-glass blend were each used for the armor backplate. These backplate materials were bonded to an exterior ceramic tile of silicon carbide to form the composite armor. In order to reduce the thermal stresses of the composite material, an intermediate rubber layer was bonded between the backplate and ceramic tile. The purpose of the rubber layer was to reduce the thermal strain mismatch near the interface due to the dissimilar coefficients of thermal expansion of the top and bottom layers by providing a more compliant layer. Experiments were conducted on several configurations of composite armor specimens exposing them to temperature ranges of $-51.1^o C\ (-60^o F)$ to $82.2^o C\ (180^o F)$. Strain gages were attached to the composite materials to determine thermal deformations and strains. In addition, finite element analyses were conducted using ANSYS 8.1 which modeled the laminar composite material. Furthermore, a theoretical model using Composite Materials Analysis of Plates (CMAP) was used to determine strains using classical laminar plate theory. Strains calculated from the finite element model and CMAP were compared to the strains from the experiment. Good agreement was attained in the comparisons of the strains in

each of the three models. The results also served to validate some material properties, but further testing is required to better characterize the properties of the S2 glass and IM7 carbon materials. Conclusions from this paper can integrate thermal effects into ballistic and other structural testing for FCS armor research.

Keywords: Future Combat System, composite armor, thermal properties, finite element analysis.

1. **Introduction**

Due to the changing nature of U.S. combat operations, a need for a more mobile and rapidly deployable armored system is required. Certain aspects of the Future Combat System (FCS) are being investigated by the Army Research Laboratory (ARL) in order to replace the M1 series Main Battle Tank. The main goal of the FCS is to significantly reduce the weight of the 70-ton M1 series tank to an armored design weighing approximately 20 tons. This reduction in weight will enable the U.S. Army to successfully conduct its stability operations in areas with poor transportation infrastructures.

In order to reduce the weight of the FCS, a Ceramic Integral Composite Armor System (CICAS) was formulated, fundamentally consisting of exterior ceramic tiles bonded to a backplate. The CICAS's ballistic performance, structural integrity, and armor crew survivability is currently under extensive testing at ARL. Since the U.S. Army and its equipment deploys to areas around the world, the equipment is invariably exposed to a wide range of temperatures. This paper focuses on the structural aspect of thermal stresses and strains in which the CICAS could potentially be exposed.

Thermal stresses in the composite armor are a concern since the armor backplate and ceramic tiles have significantly different mechanical and physical properties. The effects of mismatched coefficients of thermal expansion between the different material layers are of interest. When the layers are exposed to temperature extremes, the different coefficients of

thermal expansion cause the sandwich plies to expand and contract different amounts. When the layers are bonded together, these different amounts of thermal expansion induce thermal and mechanical strains (henceforth, collectively referred to as “thermal strains”) in the overall composite material. These thermal strains could adversely affect the performance of the composite armor by causing the composite layers to debond or undesirably impact the survivability characteristics of the composite armor.

The baseline CICAS consists of a backplate bonded to a ceramic tile. The backplate materials examined were titanium (Ti 6-4), aluminum (Al 5083), and S2-glass blend. The S2-glass blend backplate system contained a graphite layer (IM7 carbon) for structural support. The ceramic exterior tile was a silicon carbide (SiC) ceramic. An additional Ethylene Propylene Diene Monomer (EPDM) rubber interface layer was used to provide a compliant layer between the backplate and ceramic tiles; thereby, reducing the effect of the mismatch of thermal strains of the respective layers. The dimensions of the constitutive materials were four-inch squares with varying thicknesses. The silicon carbide, S2 glass blend, and aluminum materials were 0.75 inches thick. The titanium material was 0.375 inches thick. The IM7 carbon material was 0.125 inches and the EPDM rubber was 0.0625 inches in thickness.

Limited studies have been conducted in the field of thermal characterizations of composite armor systems. Previous studies focused primarily on the ballistic properties and structural integrity of composite armor. Gama et al. [1], Mahfuz et al. [2], Monib and Gillespie [3], and DeLuca et al. [4] were some of many studies of the ballistic effects on composite armor. Structural aspects of composite armor were investigated by Huang et al. [5], Dávila et al. [6, 7], and Mahdi and Gillespie [8]. However, no analyses have been conducted which characterize CICAS at below freezing and at elevated temperatures. Furthermore, the component materials of

the composite armor are only marginally characterized at temperature extremes. For example, Moy et al. [9] described the mechanical characterization of EPDM rubber at different temperature ranges, but did not analyze other mechanical and physical properties pertinent to thermal testing of composite armor.

2. **Experimental Model**

2.1. *Procedure*

Experimental thermal strains were measured in the CICAS by exposing the composite recipes to expected operational temperature ranges. The different composite configurations consisted of a silicon carbide tile coupled with a backplate consisting of titanium, aluminum, or the S2 glass blend with a graphite layer sandwiched between the glass and ceramic. A rubber interlayer between the backplate and the ceramic tile was also analyzed. Prior to laying up the composite plies, the backplate specimens and the ceramic tiles had to undergo a silane treatment to ensure that the Hysol EA9696 adhesive properly bonded the laminar plies. The first step of the silane treatment is to mix deionized water with 1% glycidoxypropyltrimethoxy silane by weight and stirring the mixture. Next, glacial acedic acid was added until a pH of 4 to 5 was achieved. The backplate specimens were then submerged in the aggregate mixture for at least one minute and then transferred to a pre-heated oven at $93^o C$ $(200^o F)$. Once the backplate and ceramic samples were cured at an elevated temperature for one hour, the specimens were allowed to cool in the oven overnight.

The silane pre-treated samples were fabricated into composite layers using lay-up. The plies were cured at $110^o C$ $\left(230^o F\right)$ for one hour and simultaneously were vacuum compressed for an extended period of time. The excess adhesive was scraped off the finished composite specimens.

Initial testing of the strain gages was required since the amount of thermal deformation which the strain gages themselves underwent was unknown. Thus, strain gages were attached to titanium silicate since this material experiences negligible thermal deformation. The strain measurements from the titanium silicate were subtracted from the specimen strain measurements in order to remove any thermal deformations which the strain gages themselves underwent. In addition, strain gages were attached to the constituent materials of the composite armor to gauge the amount of thermal expansion and contraction. In order to ensure that the strain gauge readings attained thermal equilibrium, the environmental chamber was programmed such that each target temperature (i.e. $48.9^{o}C$, $82.2^{o}C$, etc.) was sustained for a six hour period. Subsequently, the temperature was changed to the next temperature and held for another six hour period. Strain readings were recorded every three seconds during the entire programmed temperature sequence. The strain reading used for analysis demonstrated little or no fluctuation, which indicated that the material had attained thermal equilibrium. During the test, some strain readings did not register any measurements due to strain gage error or delamination of the glue.

Once the initial testing was completed, strain gages were attached to the composite armor specimens. Strain gages were placed centered on the top and bottom faces of the backplates and silicon carbide. In addition, a strain gage was placed in the center of each backplate and ceramic tile. Lastly, a strain gage was placed near the interface of each material. For the S2 glass specimens, an additional strain gage was placed on the IM7 graphite layer in order to determine the strains in the graphite layer. Figures 1, 2, and 3 show the strain gage placement for aluminum, titanium, and S2 glass composite specimens, respectively. Each specimen initially started at $15.6^{o}C$ $(72^{o}F)$ and was exposed to elevated temperatures of $48.9^{o}C$ $(120^{o}F)$ and $82.2^{o}C$ $(180^{o}F)$ in an environmental chamber. In addition, the composite recipes were exposed

to reduced temperatures of $12.2^{o}C$ $(10^{o}F)$ and $-51.1^{o}C$ $(-60^{o}F)$. Figure 4a and 4b show the environmental chamber used in this experiment and placement of specimens in the environmental chamber, respectively. The composite specimens were wrapped with a thermal blanket in order to ensure that the specimens achieved thermal equilibrium throughout the sample. In addition, the blanket served to shield the specimens from thermal shock at the surface. Strain measurements were read from the strain gages once each specimen attained thermal equilibrium.

2.2. *Results*

The experimental strains determined from the strain gages on aluminum and titanium backplates are listed in Table 1. The strain measurements for the S2 glass specimen are listed in Table 2, which has an additional strain measurement to account for the IM7 graphite layer. In order to ensure that the strain gage readings attained thermal equilibrium, the environmental chamber was programmed such that each target temperature (i.e. $48.9^{o}C$, $82.2^{o}C$) was sustained for a 6 hour period. Subsequently, the temperature was changed to the next temperature and held for another 6 hour period. Strain readings were recorded every 3 seconds during the entire programmed temperature sequence. The strain reading used for analysis demonstrated little or no fluctuation, which proved that the material had attained thermal equilibrium. During the conduct of the test, some strain readings did not register any measurements due to strain gage error or delamination of the glue. Upon conclusion of the composite testing, delamination of the rubber layer was observed in every specimen that underwent cooling temperatures. This phenomenon will be discussed later in this paper.

3. **Finite Element Model**

3.1. *Procedure*

The commercial finite element software package, ANSYS 8.1, was used to model the CICAS. A geometric model was generated which accurately depicted the dimensions of the composite specimens. Figure 5 shows the geometry of the S2 glass model. Brick elements, consisting of 8-node element 185, were used to mesh the composite layers. The material properties of the constituent layers for aluminum, titanium, and the EPDM rubber layer are listed in Table 3. Isotropic behavior and linear profiles were assumed to simplify the model. However, since the S2 glass blend and graphite layers are actual composite specimens composed of 9 separate layers with different fiber orientation, an orthotropic analysis was used for these two specific layers. The material properties for their associated orthogonal directions are listed in Table 4. The four corners of the backplate's unbonded surface were constrained in order to allow for thermal deformation. One corner node of the backplate was fixed in all translational degrees of freedom. Another node on the same edge as the fixed node was constrained in two degrees of freedom, x- and y-direction, in order to restrict rotation of the model. The remaining two nodes were constrained in the y-direction to impede the composite plates from overturning.

Once the models were properly constrained, thermal loads were applied which simulated the experiment. First, the composite armor was assumed to be cured at $110^{o}C$ and cooled to $15.6^{o}C$ in order to compute the residual strains induced in the various specimens during the curing process. Then, each model was exposed to increased temperature loads of $48.9^{o}C$ and $82.2^{o}C$. In addition, reduced temperature loads of $12.2^{o}C$ and $-51.1^{o}C$ were applied. Finally, total strain outputs were generated for each model. Figures 6 and 7 show the strain contour plots of the S2 glass specimen with and without the rubber interface layer at $48.9^{o}C$ and $82.2^{o}C$, respectively. Figures 8 and 9 show the strain contour plots of the S2 glass specimen with and without the rubber interface layer at $12.2^{o}C$ and $-51.1^{o}C$, respectively. The contour plots for

only one specimen are shown since the aluminum and titanium backplates displayed similar strain distributions.

3.2. *Results*

Strain computations generated from the finite element analysis are shown in Table 5. The strain readings were taken from the nodes which most closely matched the placement of the strain gages on the actual composite specimens. Analysis of the strain contour plots in Figures 6-11 show that the strains are symmetric in the specimen. This result was expected since the geometry of the specimen was also symmetric. Thus, the symmetric nature of the strain contour plot provided evidence that appropriate boundary conditions were placed on the composite model. Furthermore, future models could be reduced by three-fourths which would increase post-processing speed. Comparison of the strains generated in ANSYS 8.1 to the experimental data shows good correlation. The strain measurements of the experimental and finite element models were plotted on a graph depicting thickness of the specimen versus strain measurements and are shown in Figures 10 and 11 for aluminum with and without rubber, Figures 12 and 13 for titanium with and without rubber, and Figures 14 and 15 for S2 glass with and without rubber specimens, respectively.

4. Theoretical Analysis

4.1. *Procedure*

A theoretical analysis was conducted using Composite Materials Analysis of Plates (CMAP) to determine strain measurements in the composite armor specimens. CMAP incorporates standard laminated plate theory which is explained in Ashton et al. [10], R. M. Jones [11], Tsai et al. [12], and Whitney et al. [13]. Additional capabilities that CMAP offers

include determining effective laminate properties, calculating laminate stiffness, determining the laminate strengths to include residual stress failure and progressive failure, and lamina point stress/strain calculations. Diverse loading conditions can be integrated into a theoretical model ranging from in-plane force to moment resultants and hygrothermal effects [14]. This analysis could be used since analysis of the models generated in ANSYS 8.1 confirmed that the strain gages were not placed in regions where the strain distribution transitioned into nonlinear regions due to edge effects. Thus, the assumption of a plate of infinite length and a linear strain distribution are valid for these composite specimens. Utilizing the same material properties listed in Tables 3 and 4, strain calculations were generated in CMAP through the specimen thickness. The specimens containing the rubber layer were not calculated using CMAP because the use of laminar plate theory cannot accurately predict the performance of the compliant rubber layer, due to voids formed between the rubber and adjacently bonded materials.

4.2. *Results*

The strain calculations from CMAP are displayed in Table 6 for the aluminum, titanium, and S2 glass specimens without rubber. Only two strain calculations were required, one at the top and bottom faces of each constitutive material, in order to generate the strain distribution through the thickness of the material since CMAP assumes a linear strain relationship. Analysis of the CMAP model and experimental data shows good agreement for strain predictions. The experimental and CMAP strain data were graphed on a microstrain versus thickness of the composite specimen plot and are shown in Figure 10 and 11 for aluminum, Figure 12 and 13 for titanium, and Figure 14 and 15 for S2 glass specimens.

5. Discussion

Comparison of the experimental, finite element, and CMAP strain data shows good correlation between the three models. In relatively few cases, some error is observed between the experimental data and the numerical and analytical models. One major contribution to the source of error is the characterization of the material properties. Since the S2 glass material and the IM7 carbon are themselves composites composed of several layers with different fiber orientation, the accurate identification of a physical value for material properties in the orthogonal directions is extremely difficult at best. In addition, the EPDM rubber layer demonstrates elastic-plastic behavior at different temperatures. The material properties used in the numerical analysis were for the rubber at room temperature. However, since the rubber material properties are temperature dependent, different rubber characterizations were required at the different temperatures. Unfortunately, these material characterizations have not been performed for these specimens which consequently induced some error into the analytical and numerical models. Nevertheless, the good agreement of the strain data to the finite element and CMAP models show that these methods can be used to fairly predict the strains in a composite specimen and also to predict the strain trend through the thickness of the material.

Analysis of the laminar specimens with a rubber intermediate layer showed that the EPDM rubber did, indeed, provide a compliant layer which decoupled the strains between the constitutive materials (Figures 10-15). Upon the conclusion of the testing of the composite specimens, it was noted that in some instances, the rubber layer failed to remain fully intact. The Hysol EA9696 failed to create a perfect bond throughout the entire cross-section of the material specimens. As a result, the thermal free expansion of each material was compared in each of the rubber specimens. The strain graphs in Figures 10 through 15 show that the free thermal expansion prediction also provided fair agreement to the strains in the material. However, the

finite element models generated better trend predictions for the actual experimental strain data. In computing the thermal free expansion for the S2 glass and graphite composite layers, the classical computation using $\alpha\Delta T$ could not be used since the material lacked isotropic properties. Instead, CMAP was utilized to generate the effective thermal free expansion for both the S2 glass and graphite layers. Figure 15 shows the linear thermal free expansion by treating both the S2 glass and graphite specimens as an aggregate material. Thus, this collective composite material did not have the uniform free expansion of an isotropic material, but rather had a linear free expansion to account for its anisotropic properties due to the numerous layers of different fiber orientation.

During the course of testing the composite specimens, it was noted that some anomalies existed in the comparison of the strain data to the finite element and CMAP models of the aluminum specimens, primarily at $-51.1^{o}C$. This deviation between the experimental data and calculated strain data was expected since aluminum and silicon carbide have the greatest mismatch in their coefficients of thermal expansion (α). Thus, when the aluminum specimens were cooled to the temperature extreme of $-51.1^{o}C$, the mismatch in α caused extremely significant strains in the specimen which caused the Hysol EA9696 bond to break. This phenomenon was not noted in the titanium and S2 glass samples which have comparable α material properties to the silicon carbide.

6. Conclusions

The thermal strains induced in several composite armor recipes were investigated to determine whether the mismatch in thermal properties caused excessive strain and ultimately, delamination of the specimens. A numerical analysis of the thermal strains using ANSYS 8.1

and a theoretical analysis using CMAP were compared to the experimentally measured strains in the actual specimens. Conclusions from this study are as follows:

- ANSYS 8.1 finite element model demonstrated fairly accurate thermal and mechanical strain for materials with good characterizations. Experimental thermal and mechanical strains for these materials aligned well with expectations for both the FE model and the CMAP mathematical model.

- Thermal strain mismatch between materials with significantly different coefficients of thermal expansion caused delamination especially at low temperatures.

- HYSOL EA9696 failed to maintain perfect bonding between layers. Low temperature degradation of HYSOL EA9696 was observed in all experimental recipes with rubber layer.

- EPDM rubber provided a compliant layer which served to decouple the thermal and mechanical strains between the ballistic protective layer and the structural backplate layer.

- Material properties must be validated at elevated (and lowered) temperatures and non-orthogonal material property tests must be performed on S2 glass, IM7 carbon and EPDM rubber specimens.

- Coupon lay-up procedure should be standardized and manufacture of composite specimens should be within a strict tolerance.

The ANSYS 8.1 and CMAP models accurately predict the strains in the material due to thermal loads. Since the analytical and theoretical models provide good agreement with the experimental strains, these models can be used to investigate the combination of stresses and strains when a mechanical load is applied to the composite armor. Thus, the mechanical and thermal stresses and strains can be analyzed simultaneously to assist in the structural testing of the composite recipes.

References

[1] Gama, B.A., Gillespie, J.W., Bogetti, T.A., and Fink, B.K. "Innovative Design and Ballistic Performance of Lightweight Composite Integral Armor." Technology for the Army's Transformation. SAE World Congress and Exposition, Detroit, MI, March 5-8, 2001. Paper No. 2001-01-0888

[2] Mahfuz, H., Zhu, Y., Haque, A., Abutalib, A., Vaidya, U., Jeelani, S., Gama, B., Gillespie, J., and Fink, B. "Investigation of High-Velocity Impact on Integral Armor Using Finite Element Method." *International Journal of Impact Engineering*, 2000. Vol. 24(G), pp. 203-217.

[3] Monib, A.M., Gillespie, J.W. "Damage Tolerance of Composite Laminates Subjected to Ballistic Impact." Proceedings of ANTEC 98, Brookfield, CT. Society of Plastic Engineers, 1998. pp. 1463-1467.

[4] DeLuca, E., Prifti, J., Betheney, W., and Chou, S.C. "Ballistic Impact Damage of S2-Glass Reinforced Plastic Structural Armor." *Composite Science Technology*, 1998. Vol. 58(9), pp. 1453-1461.

[5] Huang, X.G., Gillespie, Jr., J.W., Kumar, V., and Gavin, L. "Mechanics of Integral Armor: Discontinuous Ceramic-Cored Sandwich Structure Under Tension and Shear." *Composite Structures*, 1996. Vol. 36, pp. 81-90.

[6] Dávila, C.G., and Chen, T.K. "CAV Tile Layer Homogenization and Parametric Study." Vehicle Structures Directorate, ARL, July 1996. (VSD NR 96-03)

[7] Dávila, C.G., Smith, C., and Lumban-Tobing, F. "Analysis of Thick Sandwich Shells with Embedded Ceramic Tiles." NASA Technical Memorandum, September 1996.

[8] Mahdi, S., and Gillespie, J.W. "Finite Element Analysis of Tile-Reinforced Composite Structural Armor Subjected to Bending Loads." Composites: Part B, 2004. Vol. 35, pp. 57-71.

[9] Moy, P., Rodriguez, G., and Ghiorse, L. "Dynamic and Mechanical Characterization of EPDM Rubber at Low and High Temperatures." 32nd International SAMPE Technical Conference, November 5-9, 2000. (pp. 372-380).

[10] Ashton, J. E., J. C. Halpin, and P. H. Petit, Primer on Composite Materials: Analysis, Technomic Publishing Co., Inc., Stamford, Connecticut, 1969.

[11] Jones, R. M., Mechanics of Composite Materials, McGraw-Hill Book Company, New York, 1975.

[12] Tsai, S. W., and H. T. Hahn, Introduction to Composite Materials, Technomic Publishing Co., Inc., Stamford, Connecticut, 1980.

References (cont)

[13] Whitney, J. M., I. M. Daniel, and R. B. Pipes, Experimental Mechanics of Fiber Reinforced Composite Materials, Society for Experimental Stress Analysis, Monograph No. 4, Brookfield Center, Connecticut, 1982.

[14] Gillespie, J.W., Jr., L. J. Shuda, B. Waibel, J. J. Garrett, and J. Snowden, “CMAP: Composite Materials Analysis of Plates," Center for Composite Materials Technical Report, CCM Report 87-45, University of Delaware, Newark, Delaware, 1987.

	Al Face (bottom)	Al Side (center)	Al Interface	SiC Interface	SiC Side (center)	SiC Face (top)
48.9^oC	656	535	353	197	90	22
82.2^oC	1503	1260	930	401	200	
12.2^oC	-748	-812	-688	-108	-60	26
-51.1^oC	-1671	-1838	-1524	-168	-156	-56

Table 1a. Experimental micro-strain readings of aluminum without rubber specimen at various temperatures.

	Al Face (bottom)	Al Side (center)	Al Interface	SiC Interface	SiC Side (center)	SiC Face (top)
48.9^oC	602	641	650	288	147	94
82.2^oC	1374	1393	1451	427	250	196
12.2^oC	-757	-760	-754	-74	-80	-66
-51.1^oC	-1614	-1663	-1587	-187	-188	-136

Table 1b. Experimental micro-strain readings of aluminum with rubber specimen at various temperatures.

	Ti Face (bottom)	Ti Side (center)	Ti Interface	SiC Interface	SiC Side (center)	SiC Face (top)
48.9^oC	256	244	133	190	154	102
82.2^oC	509	532	295	347	315	245
12.2^oC	-267	-261	-218	-137	-85	-95
-51.1^oC	-570	-752	-649	-477	-384	-398

Table 1c. Experimental micro-strain readings of titanium without rubber specimen at various temperatures.

	Ti Face (bottom)	Ti Side (center)	Ti Interface	SiC Interface	SiC Side (center)	SiC Face (top)
48.9^oC	368	307	297	93		107
82.2^oC	718	732	651	277		293
12.2^oC	-394	-307	-324	-84	-88	-71
-51.1^oC	-1008	-683	-709	-141	-200	-137

Table 1d. Experimental micro-strain readings of titanium with rubber specimen at various temperatures.

	S2 Face (bottom)	S2 Side (center)	S2 Interface	Graphite Layer	SiC Interface	SiC Side (center)	SiC Face (top)
$48.9^o C$	193	333	159	128	94	19	No Data
$82.2^o C$	428	565	358	287	186	66	No Data
$12.2^o C$	-247	-212	-194	-139	-80	-27	-50
$-51.1^o C$	-531	-650	-605	-493	-364	-42	-102

Table 2a. Experimental micro-strain readings of S2 glass without rubber specimen at various temperatures.

	S2 Face (bottom)	S2 Side (center)	S2 Interface	Graphite Layer	SiC Interface	SiC Side (center)	SiC Face (top)
$48.9^o C$	246	184	310	68	75	68	69
$82.2^o C$	558	550	672	204	189	160	171
$12.2^o C$	-233	-348	-296	-71	-70	-82	-63
$-51.1^o C$	-563	-757	-622	-157	-158	-164	-122

Table 2b. Experimental micro-strain readings of S2 glass with rubber specimen at various temperatures.

Sample Name	Young's Modulus, E (Mpsi)	Poisson's Ratio, ν	Shear Modulus, G (Mpsi)	Coefficient of Thermal Expansion, α, $\left(\frac{1}{^{o}F}\right)$
Aluminum	11.1	0.33	4.17	13.1×10^{-6}
Titanium	16.5	0.33	6.2	2.2×10^{-6}
EPDM Rubber	0.0503	0.49	n/a	320×10^{-6}

Table 3. Material properties for aluminum, titanium, and rubber constitutive layers.

Material Property	S2 Glass	IM7 Carbon (graphite)
E_x (Mpsi)	2407036	6463998
E_y (Mpsi)	1105792	981391.8
E_z (Mpsi)	2407036	7886094
ν_{xy}	0.2929213	0.2961653
ν_{yz}	0.1230398	0.2724713
ν_{xz}	0.2929213	0.2546226
G_{xy} (Mpsi)	390256.4	264385.8
G_{yz} (Mpsi)	390256.4	1770810
G_{xz} (Mpsi)	930851.9	270149.7
α_x $\left(\frac{1}{^{o}F}\right)$	4.4E-06	2.31E-6
α_y $\left(\frac{1}{^{o}F}\right)$	5.0103517E-05	5.8471487E-05
α_z $\left(\frac{1}{^{o}F}\right)$	4.4E-06	0.81E-6

Table 4. Material properties for S2 glass and IM7 carbon specimens.

	Al Face (bottom)	Al Side (center)	Al Interface	SiC Interface	SiC Side (center)	SiC Face (top)
48.9^oC	618.8	440.9	282.68	256.8	113.09	-43.77
82.2^oC	1392.31	992.09	636.06	577.79	254.46	-98.497
12.2^oC	-799.3	-569.6	-365.15	-331.72	-146.07	56.55
-51.1^oC	-1701.7	-1212.6	-777.45	-706.22	-311	120.4

Table 5a. Finite element micro-strain calculations of aluminum without rubber specimen at various temperatures.

	Al Face (bottom)	Al Side (center)	Al Interface	SiC Interface	SiC Side (center)	SiC Face (top)
48.9^oC	637.2	609	589.7	101.35	77.65	57.66
82.2^oC	1433.6	1370.36	1326.95	228.04	174.721	129.73
12.2^oC	-823	-786.8	-761.8	-130.91	-100.3	-74.47
-51.1^oC	-1752.2	-1675	-1621.9	-278.71	-213.54	-158.56

Table 5b. Finite element micro-strain calculations of aluminum with rubber specimen at various temperatures.

	Al Face (bottom)	Al Side (center)	Al Interface	SiC Interface	SiC Side (center)	SiC Face (top)
48.9^oC	222.99	182.84	162.68	165.03	91.46	160.77
82.2^oC	501.73	411.39	366.04	371.31	205.788	361.73
12.2^oC	-287.99	-236.16	-210.14	-213.16	-118.14	-207.66
-51.1^oC	-613.19	-502.76	-447.39	-453.83	-251.52	-442.12

Table 5c. Finite element micro-strain calculations of titanium without rubber specimen at various temperatures.

	Al Face (bottom)	Al Side (center)	Al Interface	SiC Interface	SiC Side (center)	SiC Face (top)
48.9^oC	292.91	290.56	292.43	86.18	74.95	283.68
82.2^oC	659.05	653.77	657.97	193.908	168.638	638.29
12.2^oC	-378.33	-375.36	-377.71	-111.32	-96.8	-366.41
-51.1^oC	-805.53	-799.06	-804.21	-237	-206.11	-780.11

Table 5d. Finite element micro-strain calculations of titanium with rubber specimen at various temperatures.

	S2 Face (bottom)	S2 Side (center)	S2 Interface	Graphite Layer	SiC Interface	SiC Side (center)	SiC Face (top)
$48.9^{o}C$	182.9	150.61	110.3	122.9	84.35	73.17	64.5
$82.2^{o}C$	411.52	338.88	248.17	276.52	189.786	164.639	145.111
$12.2^{o}C$	-236.24	-194.55	-142.48	-158.74	-108.95	-94.51	-83.3
$-51.1^{o}C$	-502.96	-414.2	-303.33	-337.97	-231.96	-201.22	-177.35

Table 5e. Finite element micro-strain calculations of S2 glass without rubber specimen at various temperatures.

	S2 Face (bottom)	S2 Side (center)	S2 Interface	Graphite Layer	SiC Interface	SiC Side (center)	SiC Face (top)
$48.9^{o}C$	191.73	166.79	145.47	185.93	82.48	73.37	66.56
$82.2^{o}C$	431.39	375.27	327.29	418.34	185.575	165.077	149.759
$12.2^{o}C$	-309.68	-291.26	-293.82	-378.49	-107.6	-96.56	-89.06
$-51.1^{o}C$	-608.99	-558.59	-539.68	-693.68	-228.22	-204.12	-187.11

Table 5f. Finite element micro-strain calculations of S2 glass with rubber specimen at various temperatures.

Distance from bottom / Temperature	0 in.	0.75 in.	1.5 in.
$48.9^{o}C$	622	277	-67
$82.2^{o}C$	1420	631	-152
$12.2^{o}C$	-807	-360	86.9
$-51.1^{o}C$	-1750	-779	188

Table 6a. CMAP micro-strain calculations of aluminum without rubber specimen at various temperatures.

Distance from bottom / Temperature	0 in.	1.137 in.
$48.9^{o}C$	251	19
$82.2^{o}C$	536	40
$12.2^{o}C$	-275	-21
$-51.1^{o}C$	-618	-46

Table 6b. CMAP micro-strain calculations of titanium without rubber specimen at various temperatures.

Distance from bottom / Temperature	0 in.	1.69 in.
$48.9^{o}C$	160	58
$82.2^{o}C$	343	123
$12.2^{o}C$	-176	-63
$-51.1^{o}C$	-395	-142

Table 6c. CMAP micro-strain calculations of S2 glass without rubber specimen at various temperatures.

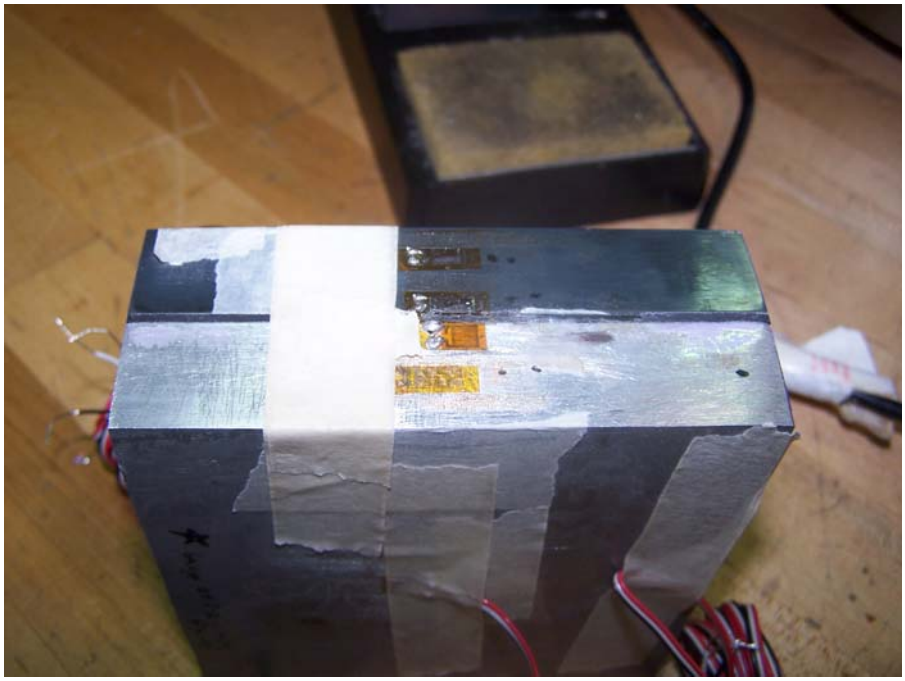

Figure 1. Placement of strain gages on aluminum composite specimen.

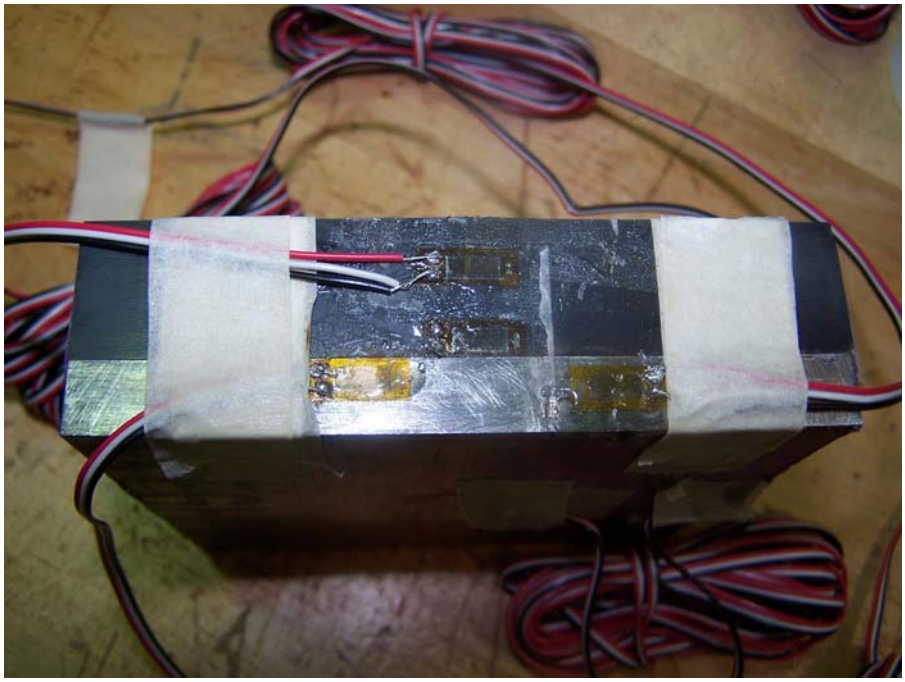

Figure 2. Placement of strain gages on titanium composite specimen.

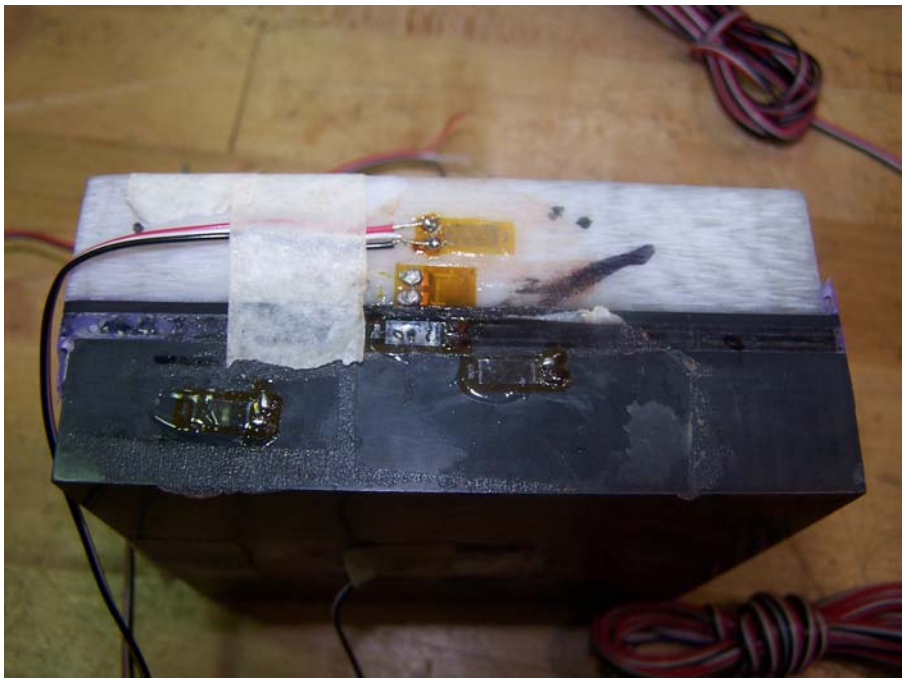

Figure 3. Placement of strain gages on S2 glass composite specimen.

Figure 4a. Picture of environmental chamber.

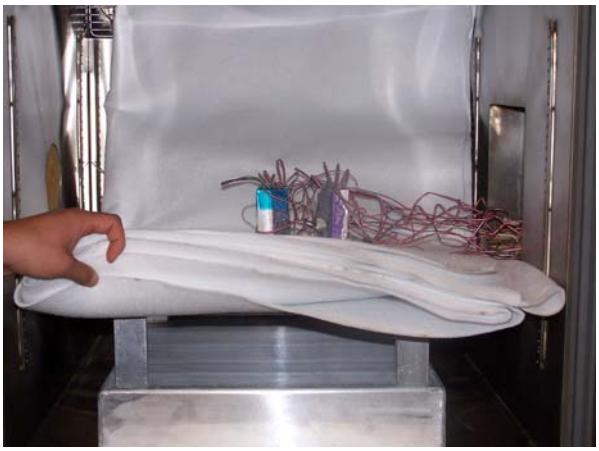

Figure 4b. Placement of specimens in environmental chamber.

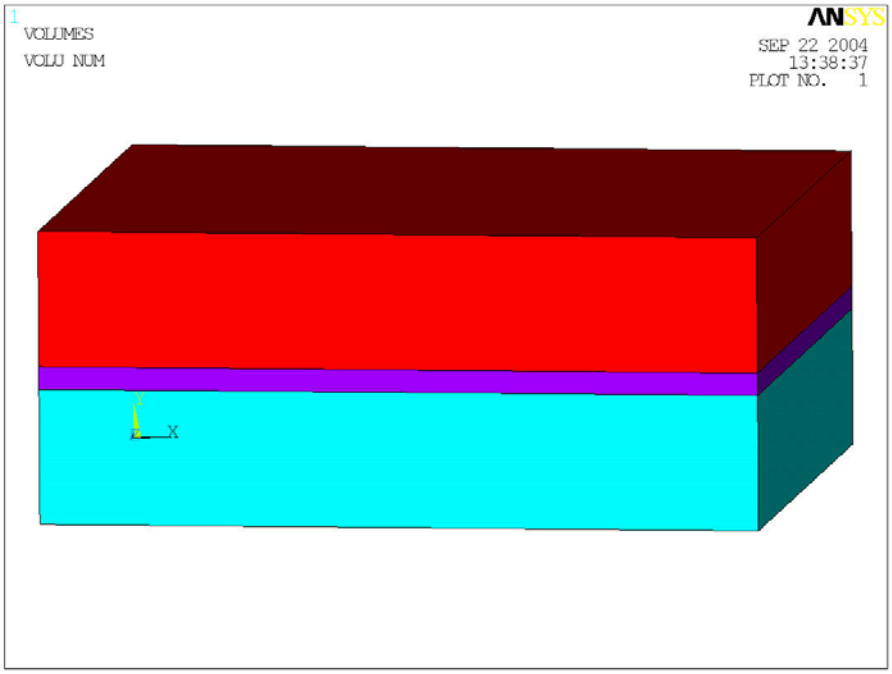

Figure 5. Undeformed model of S2 glass specimen in ANSYS 8.1.

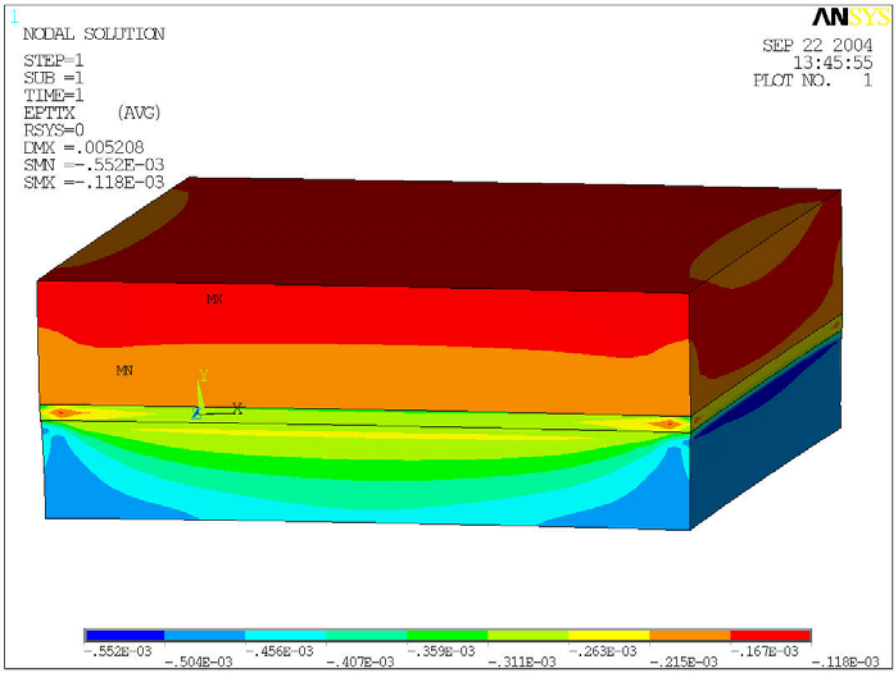

Figure 6a. Strain contour plot of S2 glass specimen at $48.9^{o}C$.

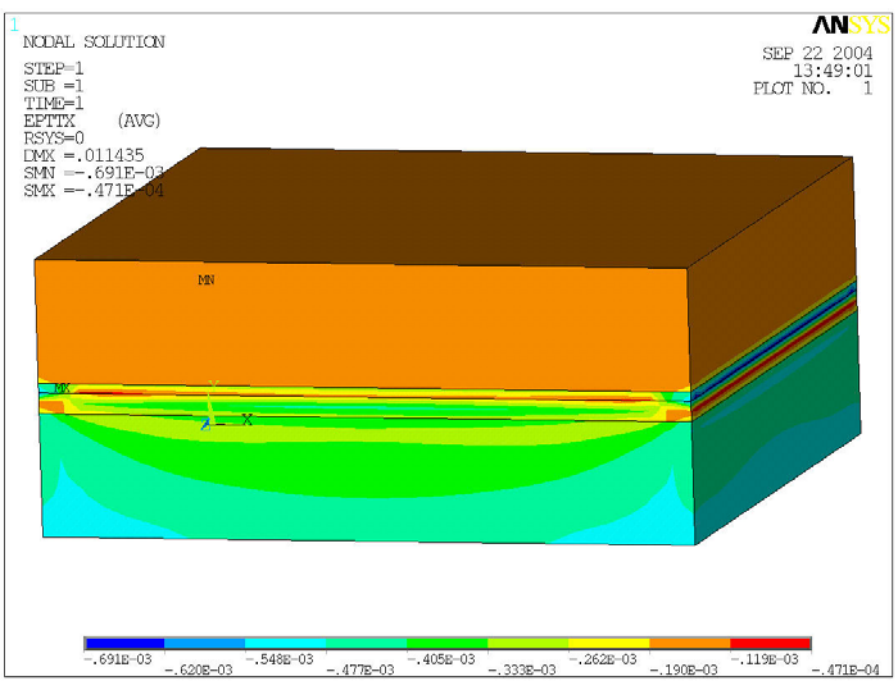

Figure 6b. Strain contour plot of S2 glass with rubber specimen at $48.9^{o}C$.

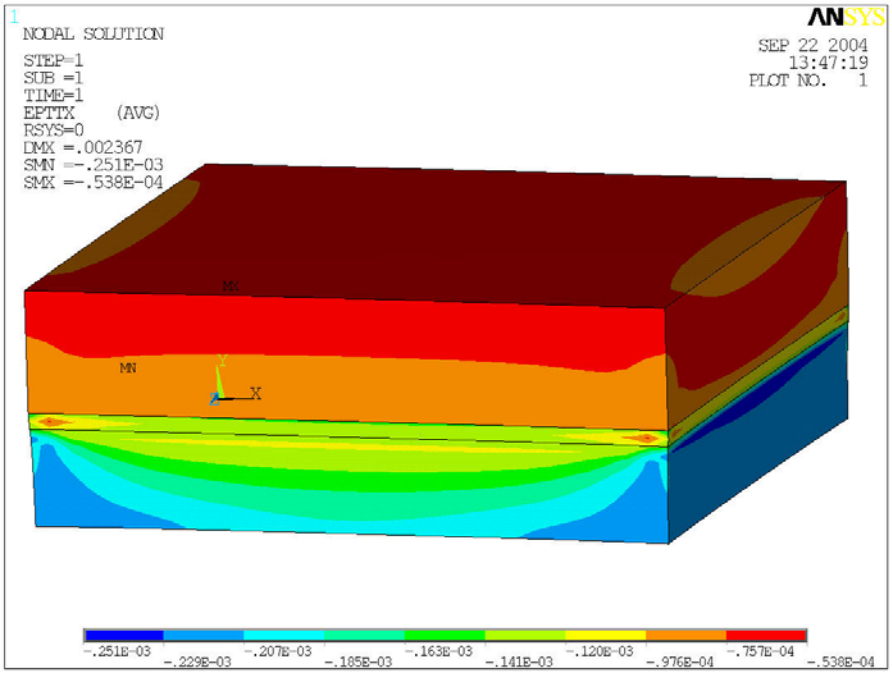

Figure 7a. Strain contour plot of S2 glass specimen at $82.2^{o}C$.

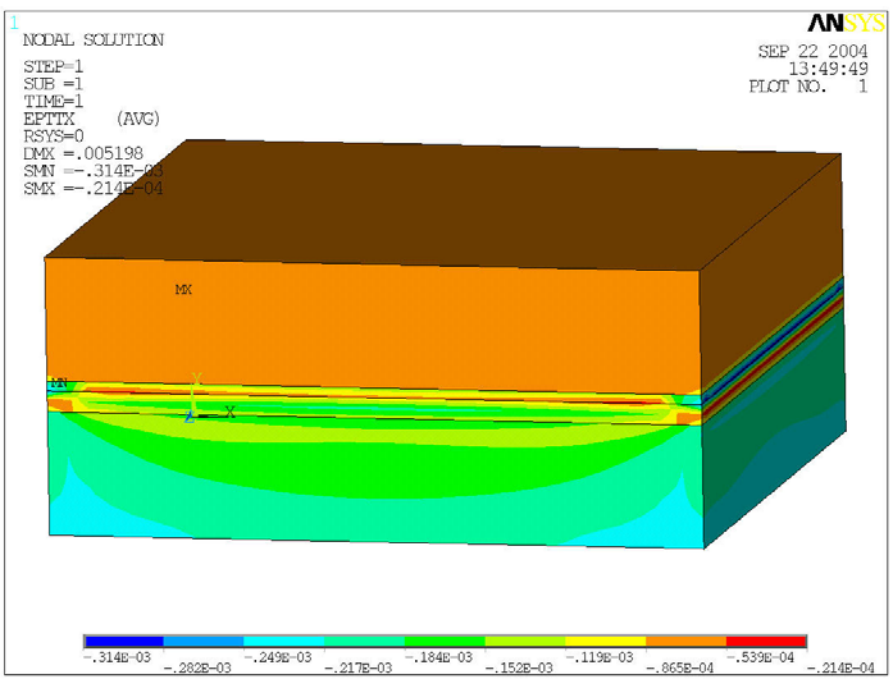

Figure 7b. Strain contour plot of S2 glass with rubber specimen at $82.2^{o}C$.

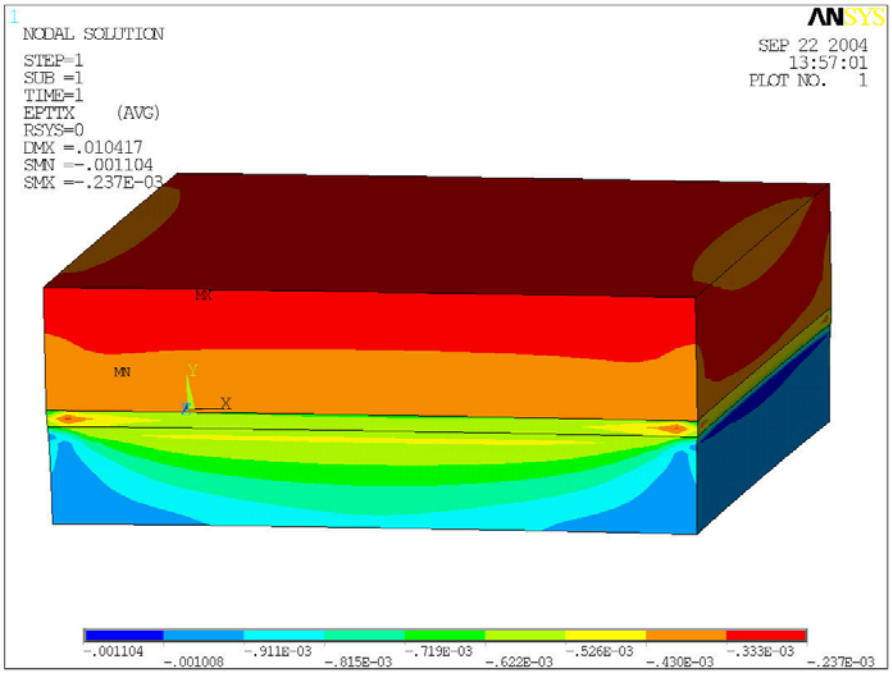

Figure 8a. Strain contour plot of S2 glass specimen at $12.2^{o}C$.

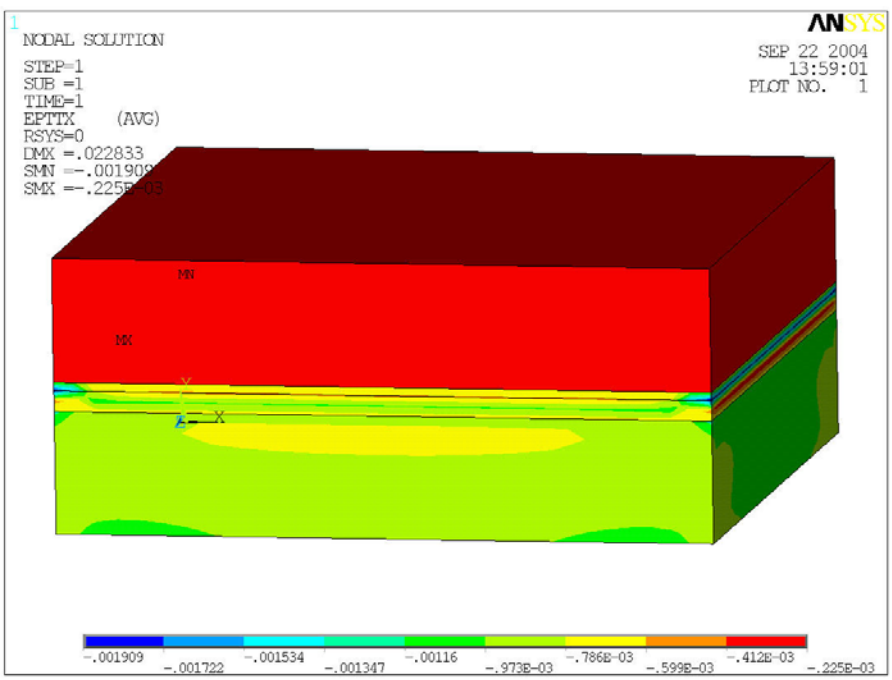

Figure 8b. Strain contour plot of S2 glass with rubber specimen at $12.2^{o}C$.

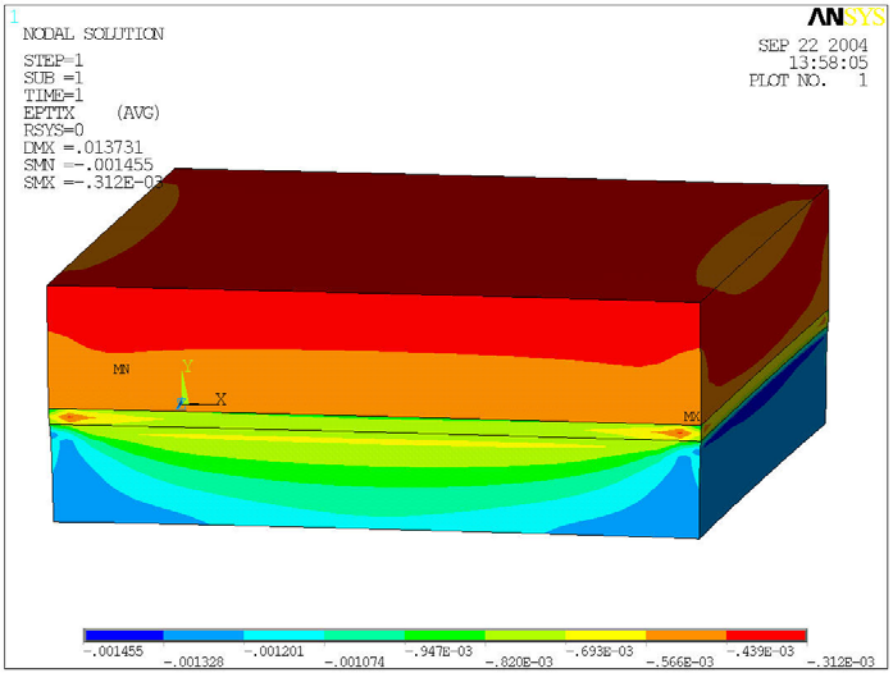

Figure 9a. Strain contour plot of S2 glass specimen at $-51.1^{o}C$.

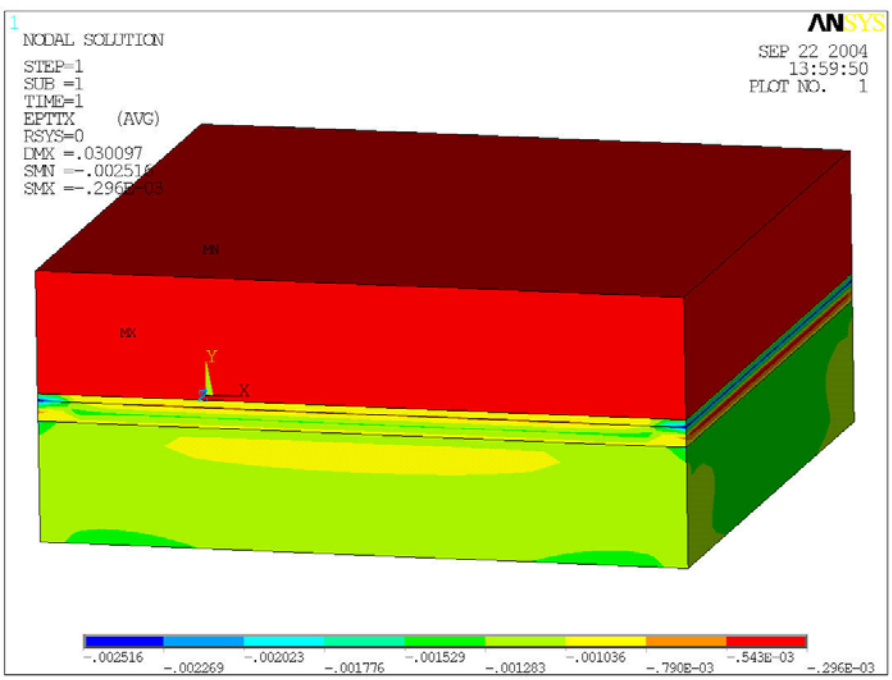

Figure 9b. Strain contour plot of S2 glass with rubber specimen at $-51.1^{o}C$.

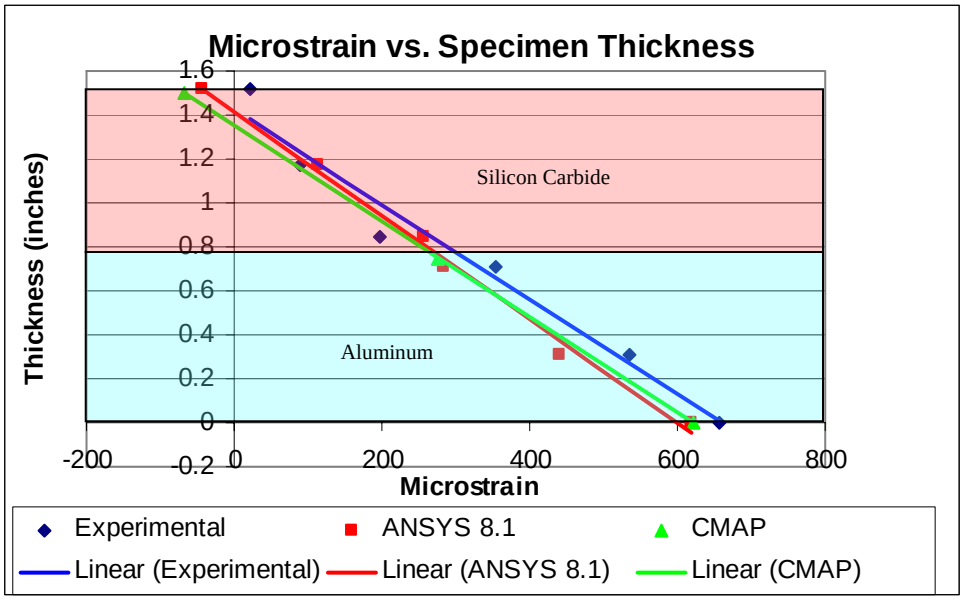

Figure 10a. Strain comparisons between experimental, finite element, and CMAP models in aluminum without rubber specimen at $48.9^{o}C$.

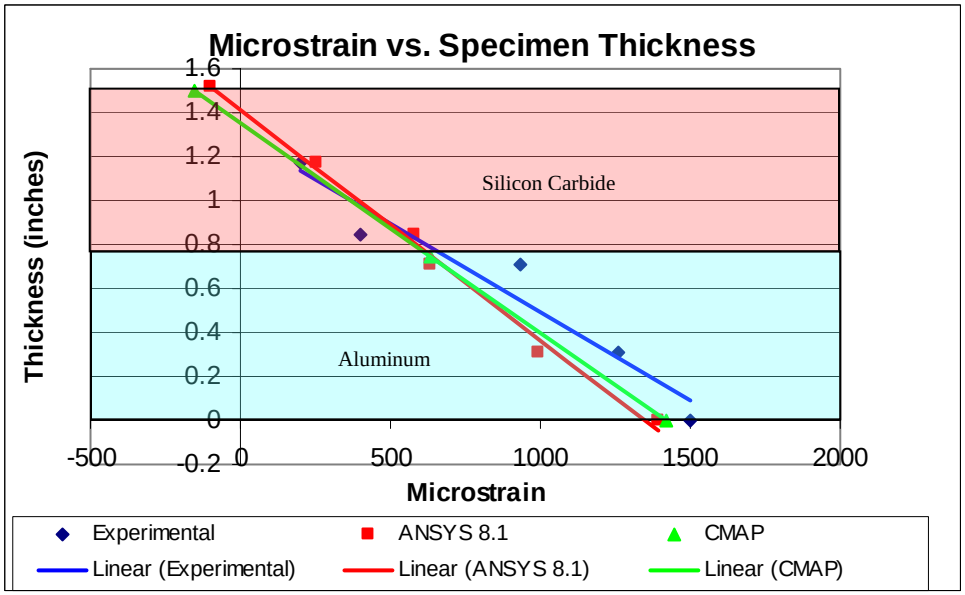

Figure 10b. Strain comparisons between experimental, finite element, and CMAP models in aluminum without rubber specimen at $82.2^{o}C$.

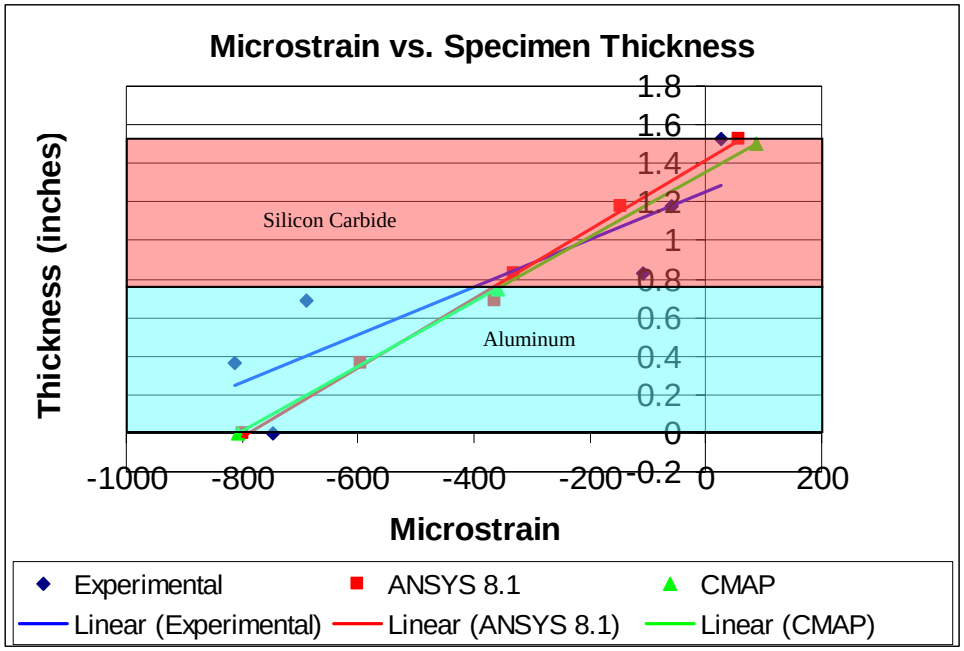

Figure 10c. Strain comparisons between experimental, finite element, and CMAP models in aluminum without rubber specimen at $12.2^{o}C$.

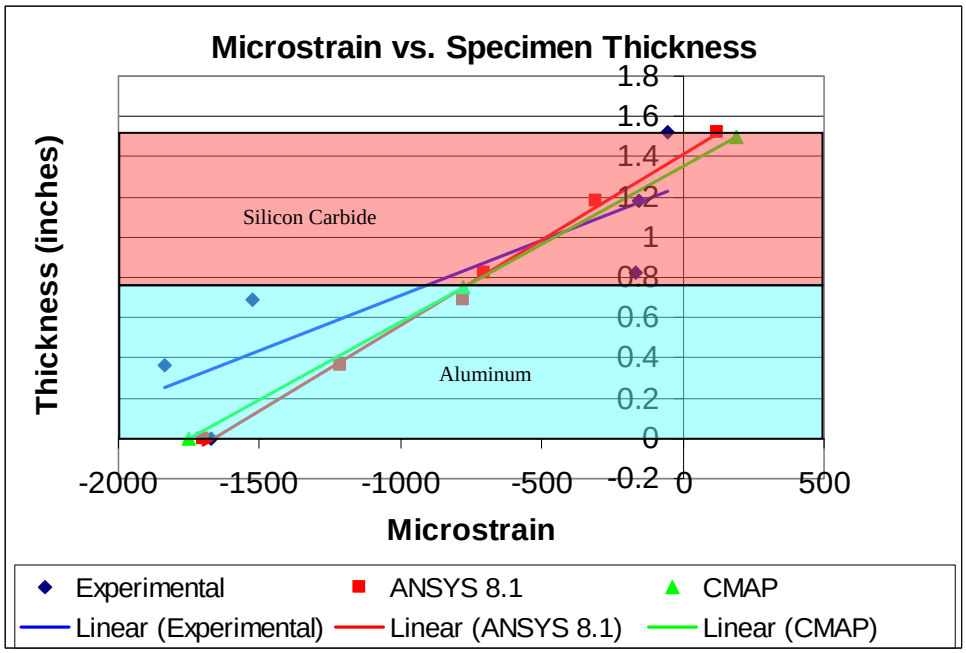

Figure 10d. Strain comparisons between experimental, finite element, and CMAP models in aluminum without rubber specimen at $-51.1^{o}C$.

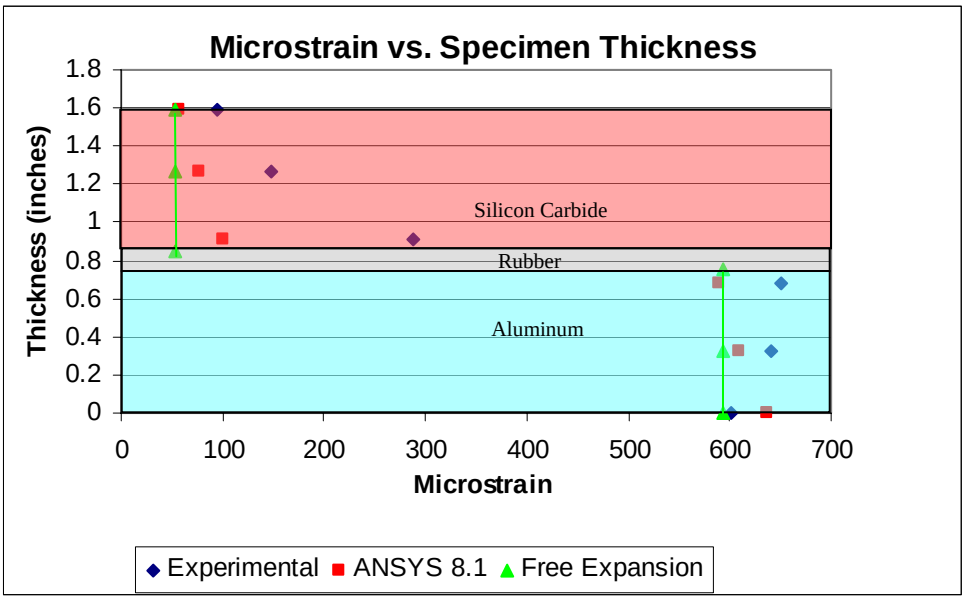

Figure 11a. Strain comparisons between experimental, finite element, and CMAP models in aluminum with rubber specimen at $48.9^{o}C$.

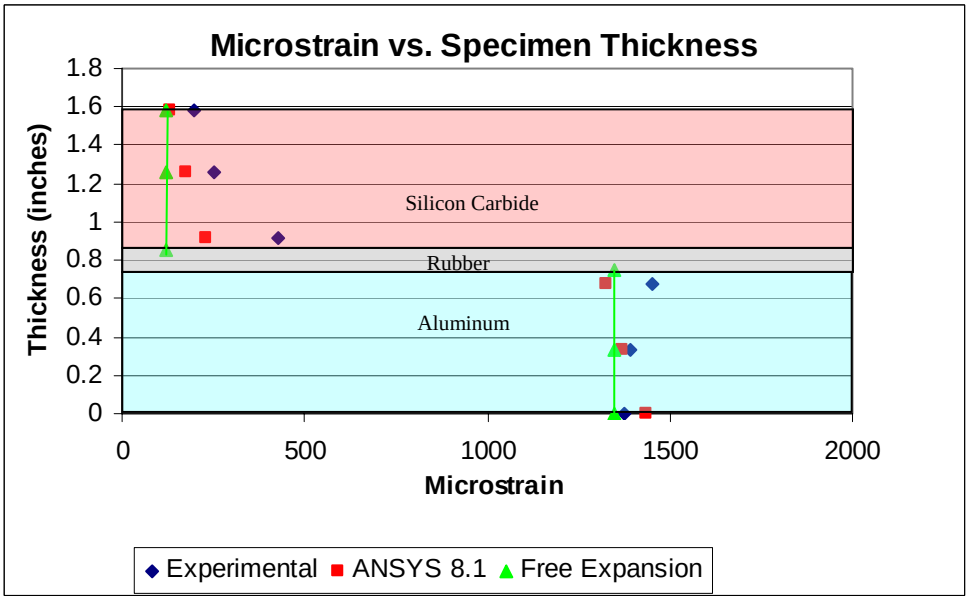

Figure 11b. Strain comparisons between experimental, finite element, and CMAP models in aluminum without rubber specimen at $82.2^{o}C$.

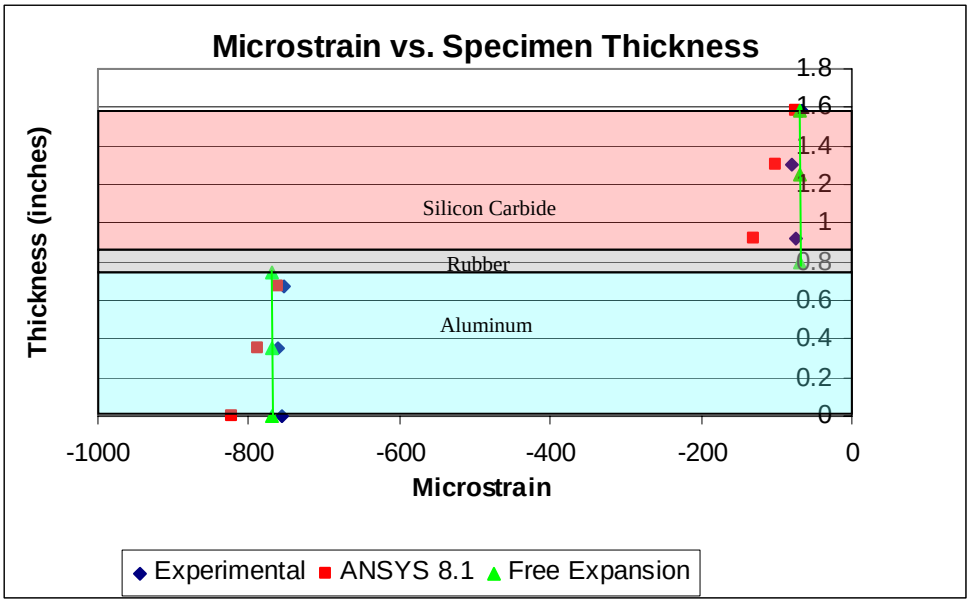

Figure 11c. Strain comparisons between experimental, finite element, and CMAP models in aluminum with rubber specimen at $12.2^{o}C$.

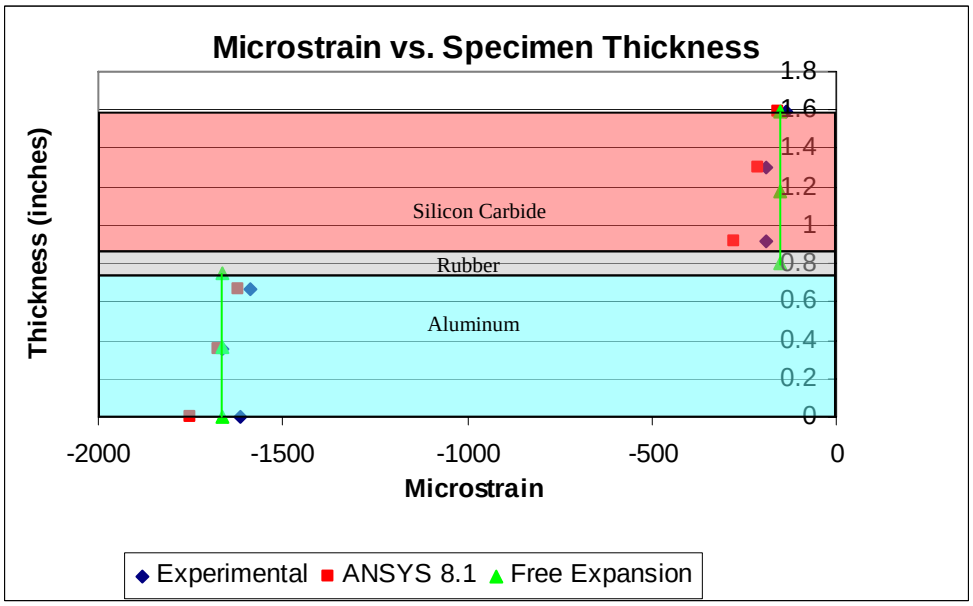

Figure 11d. Strain comparisons between experimental, finite element, and CMAP models in aluminum with rubber specimen at $-51.1^{o}C$.

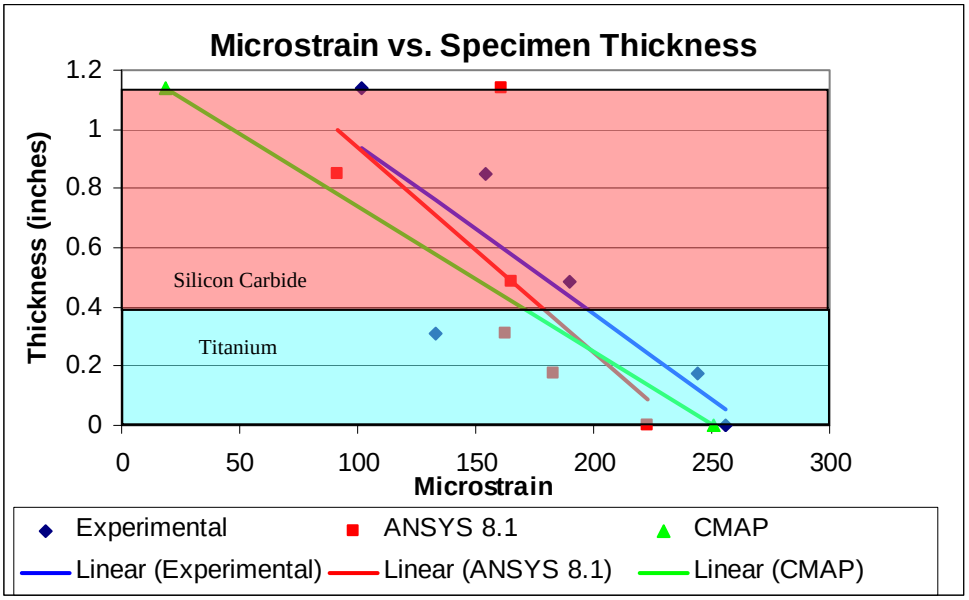

Figure 12a. Strain comparisons between experimental, finite element, and CMAP models in titanium without rubber specimen at $48.9^{o}C$.

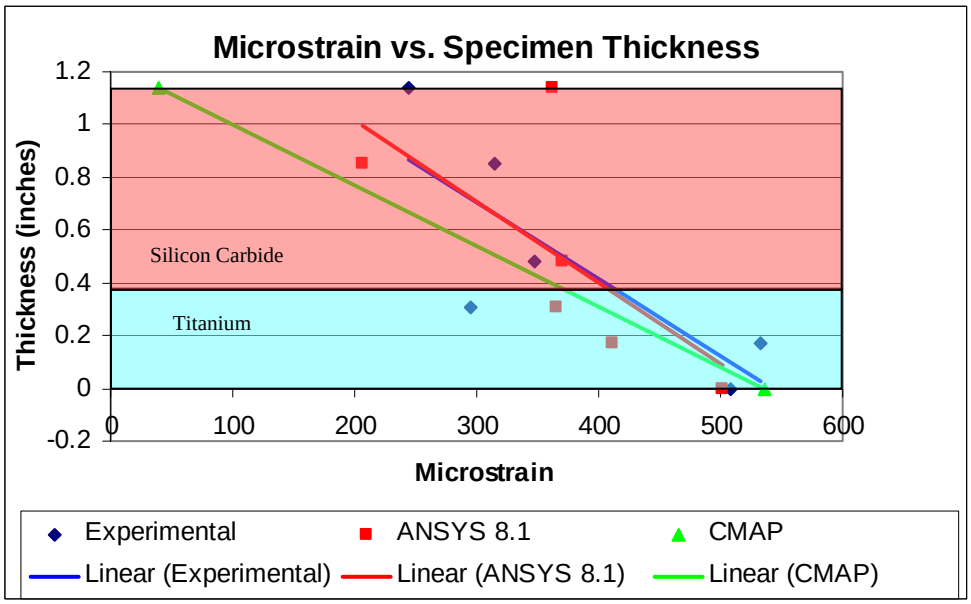

Figure 12b. Strain comparisons between experimental, finite element, and CMAP models in titanium without rubber specimen at $82.2^{o}C$.

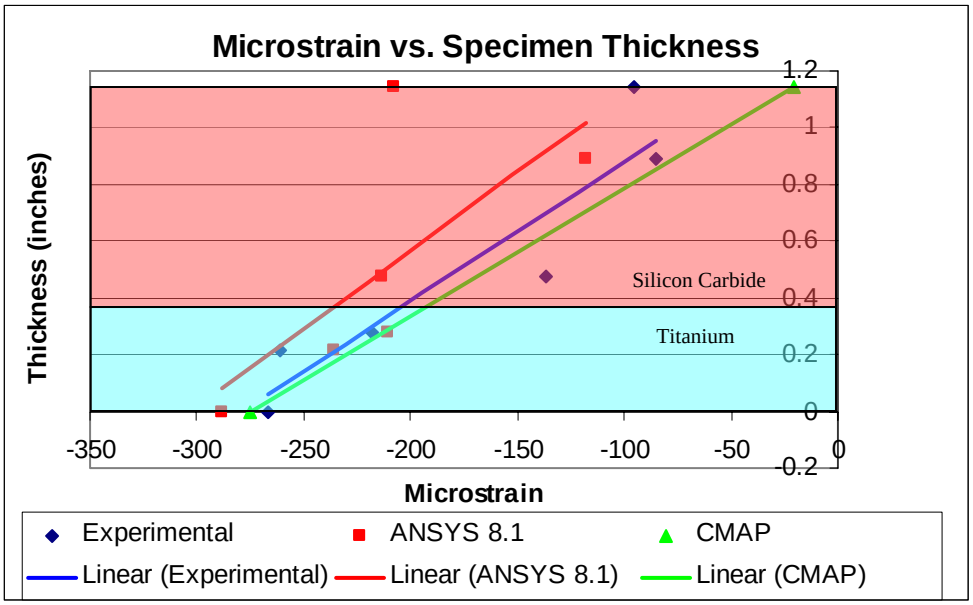

Figure 12c. Strain comparisons between experimental, finite element, and CMAP models in titanium without rubber specimen at $12.2^{o}C$.

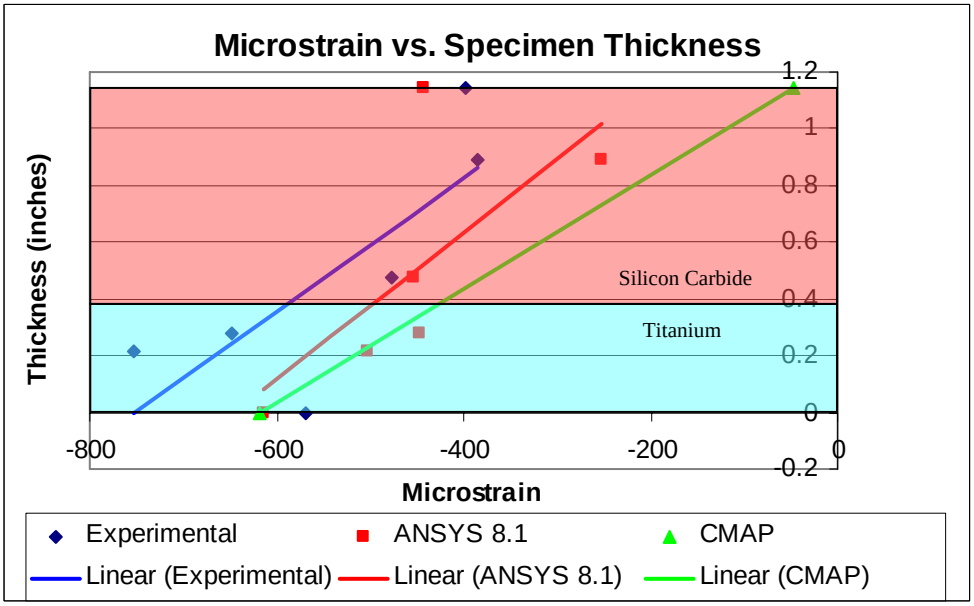

Figure 12d. Strain comparisons between experimental, finite element, and CMAP models in titanium without rubber specimen at $-51.1^{o}C$.

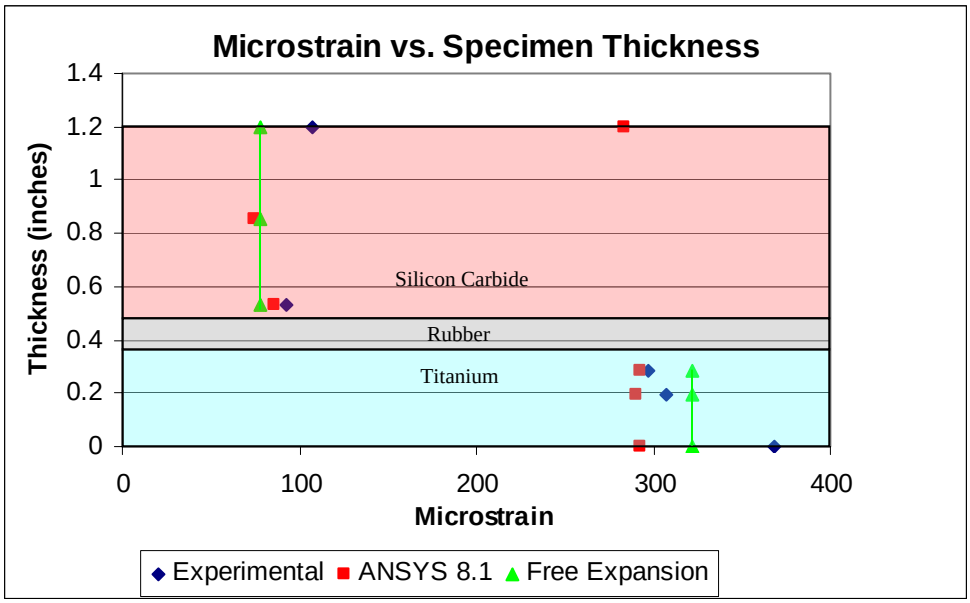

Figure 13a. Strain comparisons between experimental, finite element, and CMAP models in titanium with rubber specimen at $48.9^{o}C$.

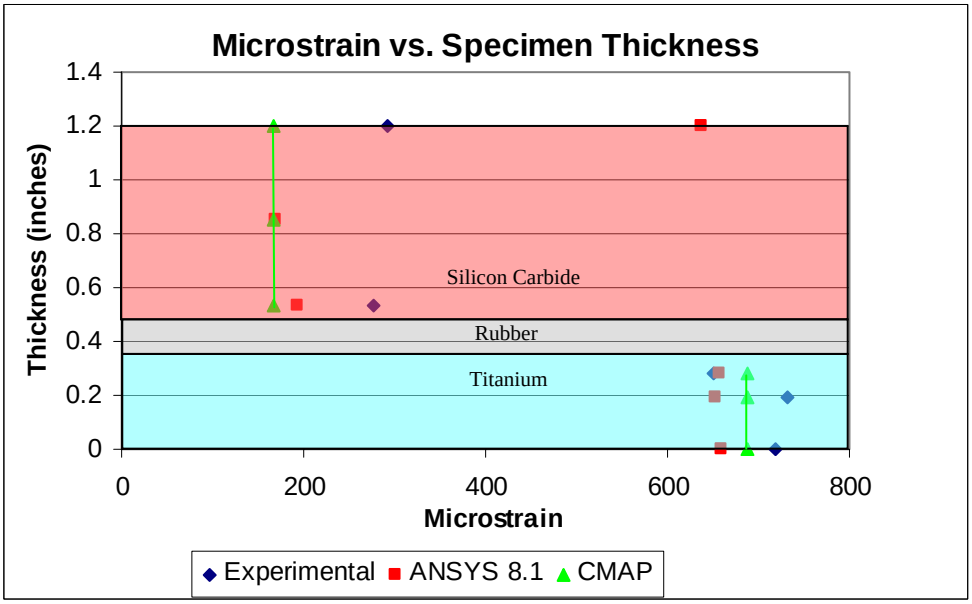

Figure 13b. Strain comparisons between experimental, finite element, and CMAP models in titanium with rubber specimen at $82.2^{o}C$.

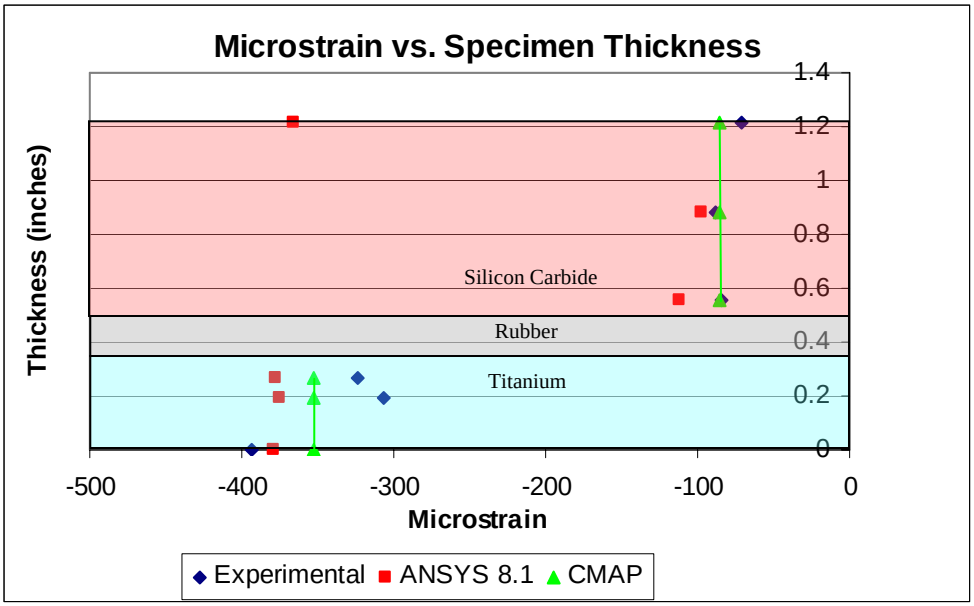

Figure 13c. Strain comparisons between experimental, finite element, and CMAP models in titanium with rubber specimen at $12.2^{o}C$.

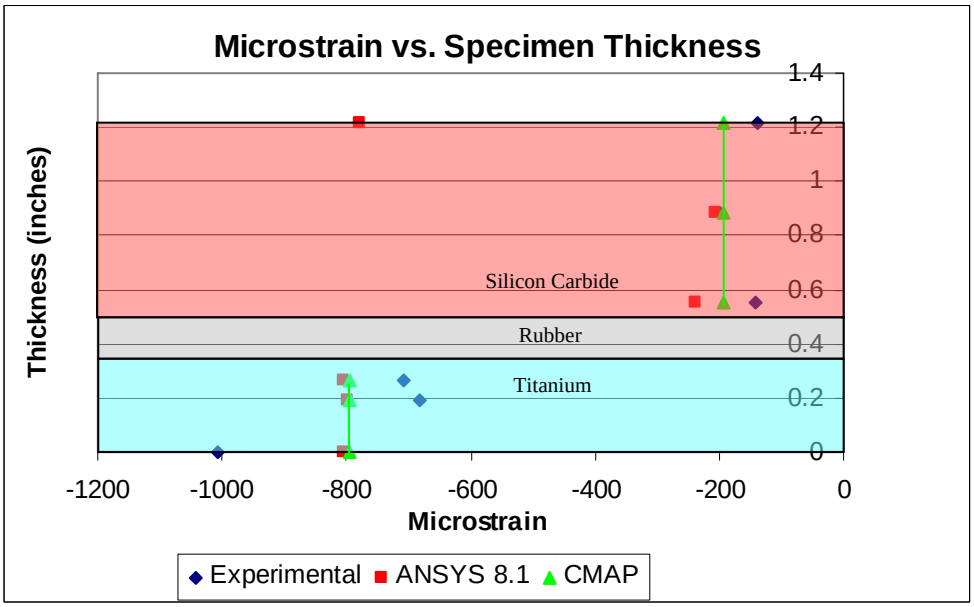

Figure 13d. Strain comparisons between experimental, finite element, and CMAP models in titanium with rubber specimen at $-51.1^{o}C$.

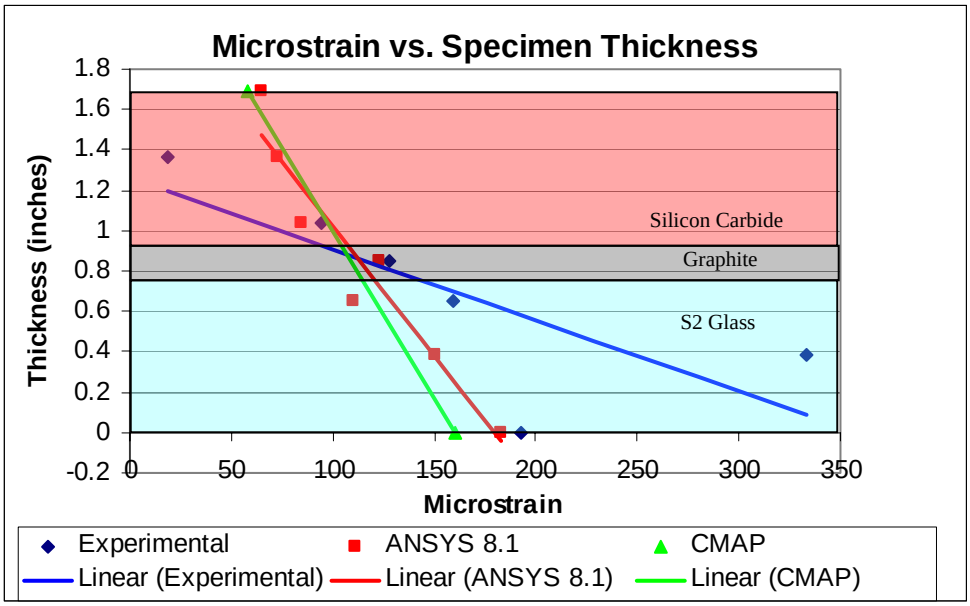

Figure 14a. Strain comparisons between experimental, finite element, and CMAP models in S2 glass without rubber specimen at $48.9^{o}C$.

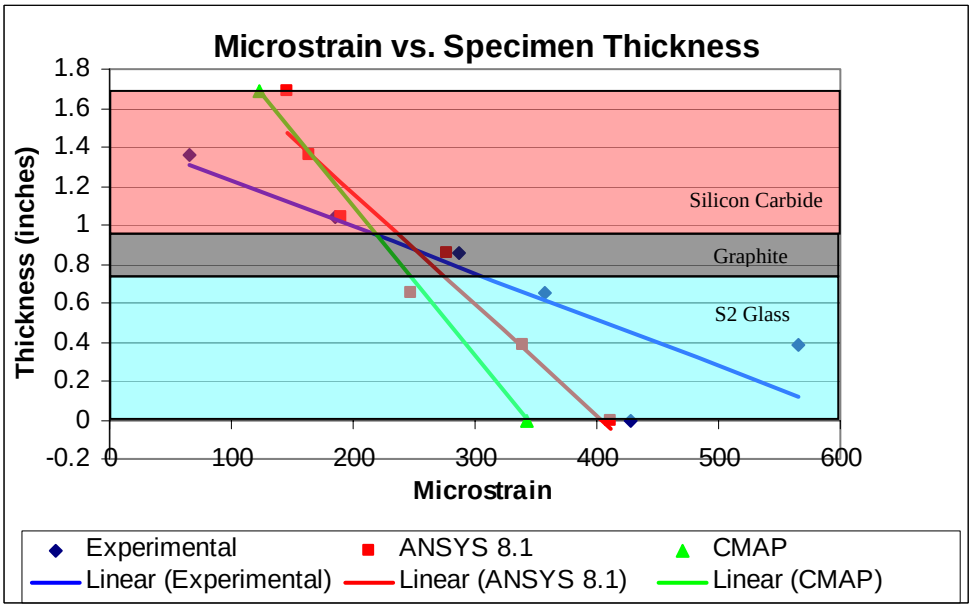

Figure 14b. Strain comparisons between experimental, finite element, and CMAP models in S2 glass without rubber specimen at $82.2^{o}C$.

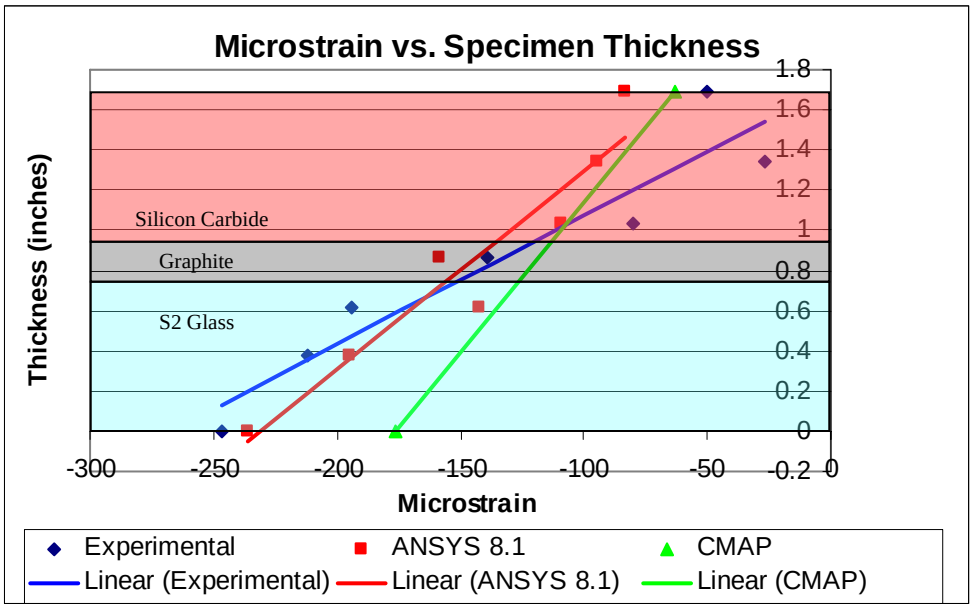

Figure 14c. Strain comparisons between experimental, finite element, and CMAP models in S2 glass without rubber specimen at $12.2^{o}C$.

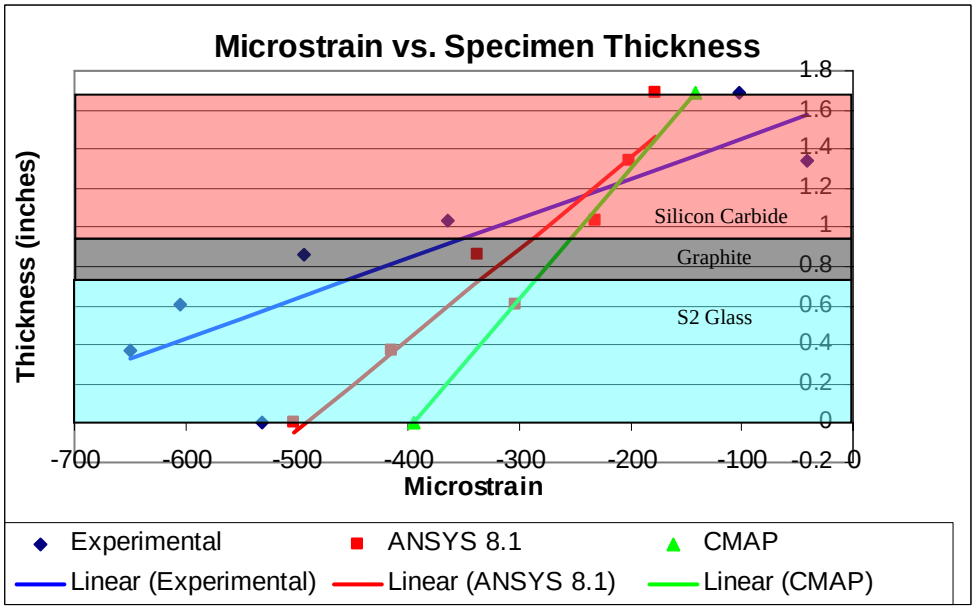

Figure 14d. Strain comparisons between experimental, finite element, and CMAP models in S2 glass without rubber specimen at $-51.1^{o}C$.

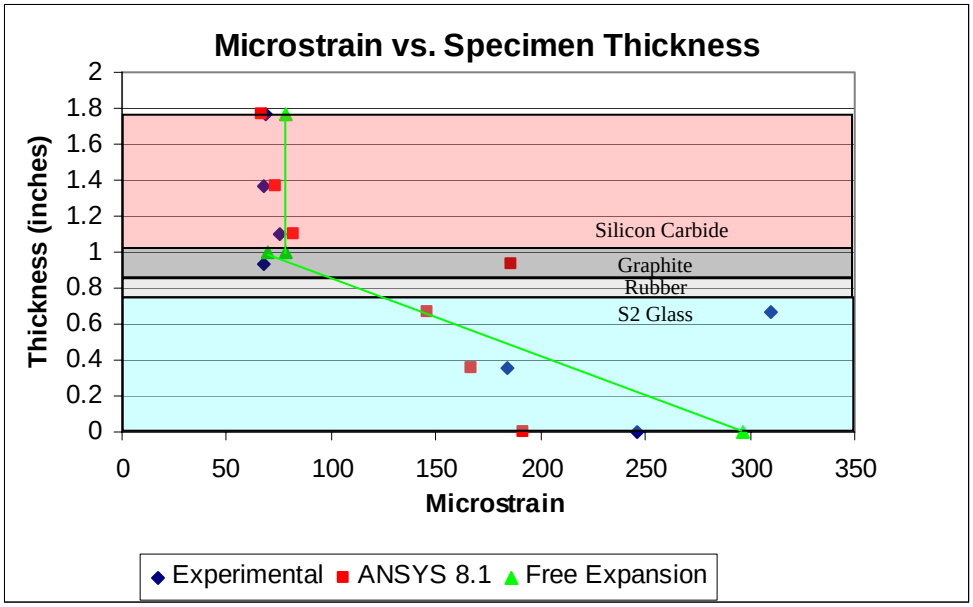

Figure 15a. Strain comparisons between experimental, finite element, and CMAP models in S2 glass with rubber specimen at $48.9^{o}C$.

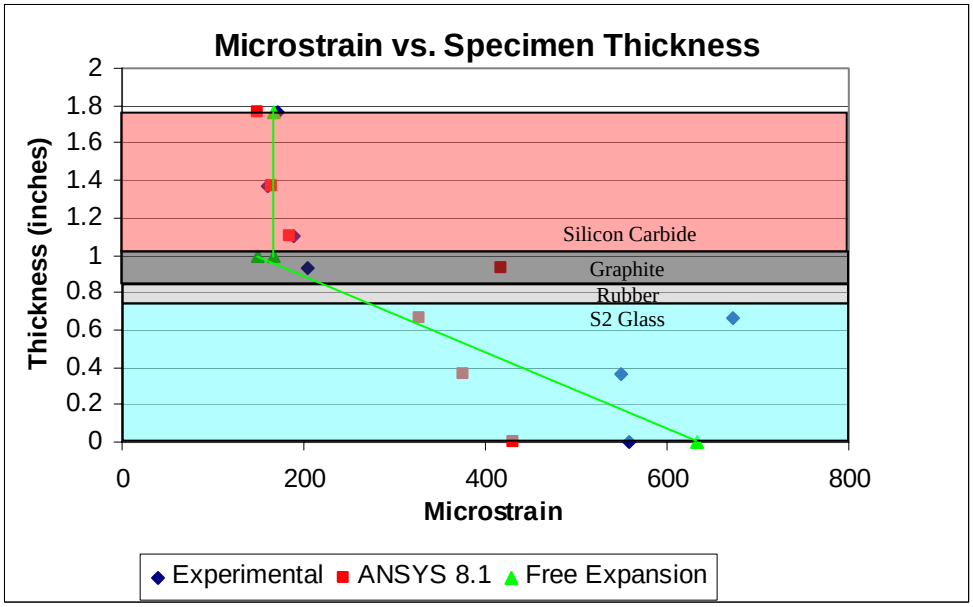

Figure 15b. Strain comparisons between experimental, finite element, and CMAP models in S2 glass with rubber specimen at $82.2^{o}C$.

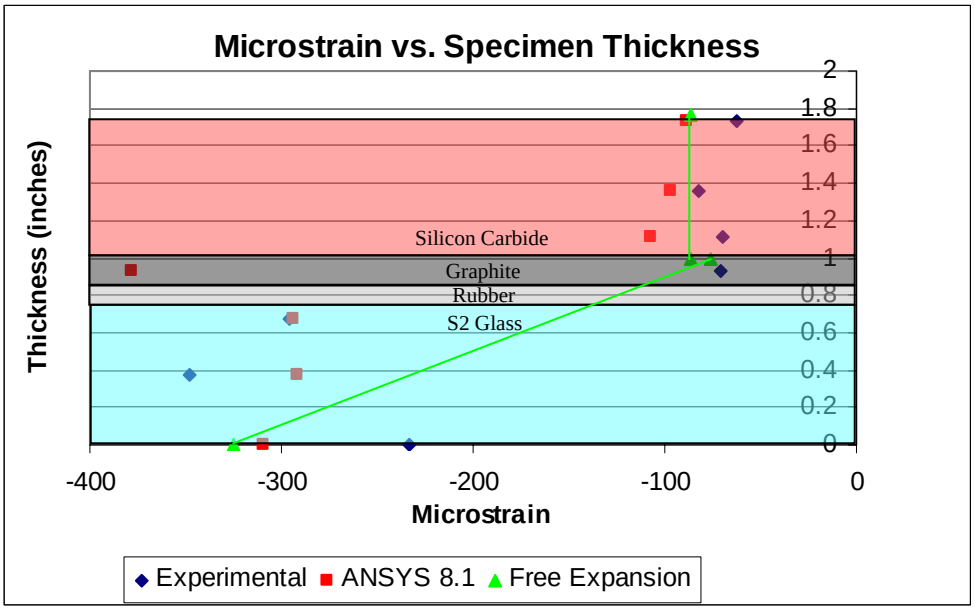

Figure 15c. Strain comparisons between experimental, finite element, and CMAP models in S2 glass with rubber specimen at $12.2^{o}C$.

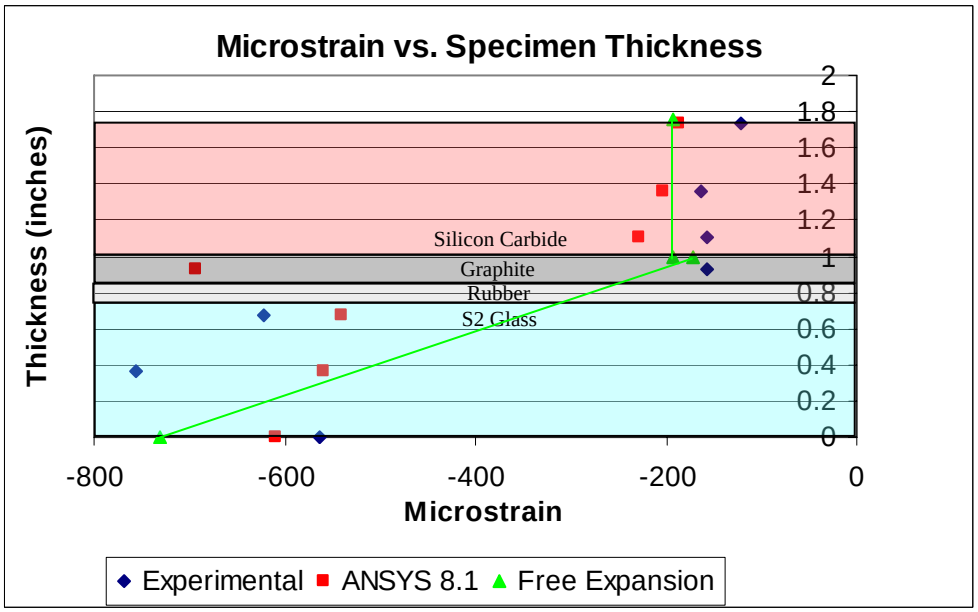

Figure 15b. Strain comparisons between experimental, finite element, and CMAP models in S2 glass with rubber specimen at $-51.1^{o}C$.